Experimental and numerical methodologies to characterize base bleed operation in internal ballistics conditions

Thomas Gaillard, Robin William Devillers, Demarthon Romain, Settie Heddadj, Hervé Le Boursicaud, Jean-Yves Lestrade, Jean-Sébastien Schwartz, Christophe Grignon, Nicolas Teyssier, Pauline Fougeroux

Experimental and numerical methodologies to characterize base bleed operation in internal ballistics conditions

Thomas Gaillard, Robin Devillers
DMPE, ONERA, Université Paris Saclay, F-91123 Palaiseau, France

Romain Demarthon, Settie Heddadj, Hervé Le Boursicaud
Nexter Munitions – 7 route de Guerry – 18000 Bourges

Jean-Yves Lestrade
ONERA / DMPE, Université de Toulouse, F-31055 Toulouse, France

Jean-Sébastien Schwartz, Christophe Grignon, Nicolas Teyssier, Pauline Fougeroux
DGA Techniques Terrestres, Rocade Est – Echangeur de Guerry, 18021 Bourges Cedex

1 Abbreviations

BB: Base Bleed
BC: Base Bleed Composition
CFD: Computational Fluid Dynamics
DL: Digital Level
HPV: High Pressure Vessel
IB: Internal Ballistics
IR: Infrared
IS: Ignition Simulator
SP: Solid Propellant

2 Notations

A_p	Pre-exponential constant [$m \cdot s^{-1}$]	R	Universal gas constant [$J \cdot mol^{-1} \cdot K^{-1}$]
a_c	Cohesion term [$m^5 \cdot s^{-2} \cdot kg^{-1}$]	T	Temperature [K]
b	Effusivity [$W \cdot K^{-1} \cdot m^{-2} \cdot s^{1/2}$]	T_{burn}	Burning temperature [K]
C’	Initial volume available for gases in the cannon, including volumes of combustible parts [m^3]	T_c	Critical temperature [K]
c	Heat capacity of a solid [$J \cdot kg^{-1} \cdot K^{-1}$]	T_f	Flame temperature [K]
c_p	Heat capacity at constant pressure [$J \cdot kg^{-1} \cdot K^{-1}$]	T_{ign}	Ignition temperature [K]
de/dt	Regression rate [$m \cdot s^{-1}$]	T_{pyr}	Pyrolysis temperature [K]
E_p	Activation energy of reactions [$J \cdot mol^{-1}$]	T_s	Surface temperature [K]
f	Force of a composition [$J \cdot kg^{-1}$]	t	Time [s]
L	Arbitrary length for the simulation [m]	t_0	Firing instant [s]
$\dot{m}$	Mass flux [$kg \cdot m^{-2} \cdot s^{-1}$]	t_{ign}	Ignition time [s]
P	Pressure [Pa]	v	Specific volume [$m^3 \cdot kg^{-1}$]
P_c	Critical pressure [Pa]	v_0	Regression rate from Vieille’s law [$m \cdot s^{-1}$]
P_{max}	Maximum pressure [Pa]	W	Molar mass [$kg \cdot mol^{-1}$]
Q_s	Heat of reaction [$J \cdot kg^{-1}$]		

Δ	Density in the HPV [$kg \cdot m^{-3}$]	μ	Dynamic viscosity [$kg \cdot m^{-1} \cdot s^{-1}$]
δ_f	Flame thickness [m]	ρ	Density [$kg \cdot m^{-3}$]
ε_s	Surface emissivity	ρ_p	SP density [$kg \cdot m^{-3}$]
η	Covolume [$m^3 \cdot kg^{-1}$]	Φ_{laser}	Absorbed laser flux [$W \cdot m^{-2}$]
λ	Thermal conductivity [$W \cdot K^{-1}$]		

3 Introduction

This study is applied to shells fired from long-range artillery systems. The first phase of a shell ballistics is called Internal (or Interior) Ballistics (IB) [1]. During this phase, the cannon shot triggers the ignition and combustion of the propellant charges in the combustion chamber (between the breech

and the shell base). Such combustion makes it possible to produce powder gases at high pressure and temperature, which set the shell in motion. The objective of this phase is to produce the highest muzzle velocity of the shell to ensure maximum range.

The usual studies performed on this phase consist in optimizing the energy release as a function of time. The objective is to obtain a good balance between the pressure increase and the chamber volume increase due to the movement of the shell, and thus avoid strong pressure waves that could damage the cannon. This involves in particular using powder grains whose shape and composition are in accordance with the intended application. From a numerical point of view, dedicated models and tools have been developed [2][3][4][5] to predict the correct pressure increase and the correct muzzle velocity of the shell. Experimental data from pressure sensors located inside a cannon make it possible to adjust and validate the simulations [6].

To verify that powder grains burn as expected, an experimental device called “Ignition Simulator” (IS), or “gun simulator”, has been developed. The IS design usually enables to reproduce the similar combustion conditions as those met during the IB first moments. The chamber volume must initially correspond to the volume in the cannon that is available for gases (usually written C'). The chamber case is generally transparent (fully transparent or made of a filament wound [7]) in order to observe the movement of the burning grains with suitable optical diagnostics. At some point of the IB cycle, the chamber case breaks due to the fact that the chamber pressure exceeds a threshold linked to the mechanical properties of the chamber case. Such device is used for example to test different ignition systems and observe flame spreading in LOVA powder grains with high-speed cameras [8][7]. The IS design allows it to be very modular to study different kind of interactions (between ignition compositions or ignition devices and one powder grain or a full loading of the chamber case) for a wide range of calibers (from 40 mm to 155 mm) [7].

After IB, begins the free flight phase of the shell outside the cannon, called external ballistics (or exterior ballistics). In order to increase the range of a gyrostabilized shell, it is necessary to decrease its drag as much as possible. The shell total drag is usually divided into several contributions (form drag or pressure drag, wave drag and viscous drag). It is form drag which generally represents more than 50% of the total drag in subsonic and supersonic regimes (between Mach 0.5 and 3) due to the pressure difference between the shell nose and base [9]. In that case, form drag can be explicitly named base drag. In order to compensate part of the base drag and increase range, the Base Bleed (BB) is a device which is now commonly used and has been widely studied around the world with both numerical and experimental activities (references [10] to [18]). Its goal is to expel a small mass flow rate of hot gases into the low pressure area at the shell base to increase pressure and then reduce base drag. More precisely, gas generation from the BB is here achieved by the combustion of a Solid Propellant (SP) unit (called BC for Base Bleed Composition in the following).

For a shell equipped with a BB, IB is all the more critical because heat transfers take place between the hot flow of powder gases and the surface of the BC. These heat transfers then lead to BB ignition and combustion. In order to better understand the phenomena occurring during IB, from the BB point of view, experimental characterizations of BB ignition and combustion are carried out and presented in this paper, as well as numerical simulations.

From the experimental side, the first ignition characterization that is presented in section 4 consists in generating a laser flux on the surface of a small SP sample and determining, using appropriate optical diagnostics, the ignition delay of the sample when absorbing this thermal stress [19]. This preliminary step makes it possible to obtain a relationship between the ignition delay and the heat flux absorbed at the surface, as shown in references [19] to [23]. When the SP is ignited, it is useful to measure its regression rate [24] in order to characterize the produced mass flow rate. For a BB, it is essential to know what the remaining mass is when it exits the cannon muzzle because it determines its effective operation during external ballistics. More specifically, as the BB might be ignited during IB, the regression rate must be characterized for very high pressures as done for example in references [25]

to [29]. For the latest purpose, a quantification of the high pressure regression rate has been performed in a dedicated experiment and presented in section 5. A second ignition characterization presented in section 6 is experimentally obtained in the IS in order to study the BB behavior under a high heat flux generated in conditions nearly similar to IB ones.

From the computational side, numerical simulations consist in using all the obtained experimental results to model the BB behavior during IB. A CFD-type simulation, solving the Navier-Stokes equations, is produced in section 7 in order to model the penetration of the powder gases flow into the BB. A SP ignition model (see for example references [30] to [32]) must be used and is generally parameterized according to experimental ignition results. The purpose of CFD is in particular to determine whether or not the BB actually ignites during IB, and also to evaluate, in the former case, the burnt propellant mass.

4 Measurement of ignition delay on BC small samples

The first experimental characterization is performed with small samples of the BC in a small combustion chamber operated at ONERA Palaiseau. The objective is to determine a relationship between an absorbed laser flux on a sample surface and the ignition delay of the sample. This relationship will be used in section 7 to provide parameters for the ignition model in order to perform numerical simulations.

4.1 Ignition phenomenology

Ignition of a SP involves heating of its surface with an external heat source (here a laser). Before ignition (meaning the onset of chemical reactions that produce a flame), the SP sample first heats up like a mere inert material [19][31][33]. The surface temperature evolution $T_s(t)$ can be modelled assuming that the SP sample is a semi-infinite 1D medium under a constant heat flux. Additional assumptions (SP with homogeneous properties, temperature-independent thermal properties) enable to express $T_s(t)$ by the following equation:

$$T_s(t)-T_s(0)=\frac{2}{b\sqrt{\pi}}\Phi_{laser}\sqrt{t} \quad (1)$$

where $T_s(0)$ is the initial surface temperature before heating starts, b is the SP thermal effusivity, Φ_{laser} is the absorbed laser flux at the BC surface. Hence, the surface temperature $T_s(t)$ follows a square root function of time t.

Above a certain temperature, pyrolysis phenomena start in the SP and induce a steeper temperature increase than an inert heating [19][31][32]. The threshold temperature at which pyrolysis starts is called the pyrolysis temperature T_{pyr} and usually sits between approximately 500 and 700 K, depending on composition and pressure. During pyrolysis, gaseous species start being released from the surface. When T_s reaches the ignition temperature T_{ign} at the instant t_{ign}, chemical reactions between the gaseous species are triggered, producing a flame close to the surface. T_{ign} is generally estimated between 600 to 800 K. Finally, the now-burning surface stabilizes at a temperature T_{burn}, which is usually found between 800 and 1200 K for usual composite SP. Once combustion has started, it becomes self-sustained without external heat input, until the entire SP has been consumed. The objective of an ignition campaign is therefore to provide $T_s(t)$ curves for different heat flux Φ_{laser}, with the best possible accuracy. Visualizations also enable to observe the flame appearance and then to deduce t_{ign}. In a real system, heating usually comes from a dedicated ignition device or from the heating of surrounding burnt gases.

4.2 Experimental setup

4.2.1 Combustion conditions

Ignition tests are carried out in a combustion chamber, located at ONERA Palaiseau [19] (see Figure 1). This chamber has an internal volume of approximately 1 liter and can be pressurized with N_2 up to 15 bar. The present tests were carried out with an initial absolute pressure of 4.5 bar of N_2. Several optical accesses are arranged on the chamber:

• portholes on the side faces (left and right), allowing the observation of the samples combustion;

• a porthole on the upper side, providing access to a laser beam which ignites the samples.

Figure 1: Combustion chamber used for the ignition campaign.

The samples are extracted directly from a real BC. Samples ignition is achieved with the irradiation of a sample surface by a high-power CO_2 laser beam with a wavelength of 10.6 µm.

4.2.2 IR measurement devices

Two infrared (IR) cameras are used to study the surface temperature evolution $T_s(t)$ during the ignition phase. They are arranged on either side of the chamber (as shown in Figure 2) at an angle between 40° and 50° with respect to the horizontal plane. The use of two cameras makes it possible to optimize the acquisition conditions over the entire temperature range corresponding to the ignition phase, namely from 300 to 700 K approximately.

A FLIR Titanium camera enables to access the first moments of the heating phase. It provides measurements between 300 and 400 K approximately. It is generally used for temperatures close to ambient.

A NOXANT camera is dedicated to higher temperatures from 500 to 700 K. Under these conditions, the camera also has the capacity to access ambient temperatures, but with a greater noise level.

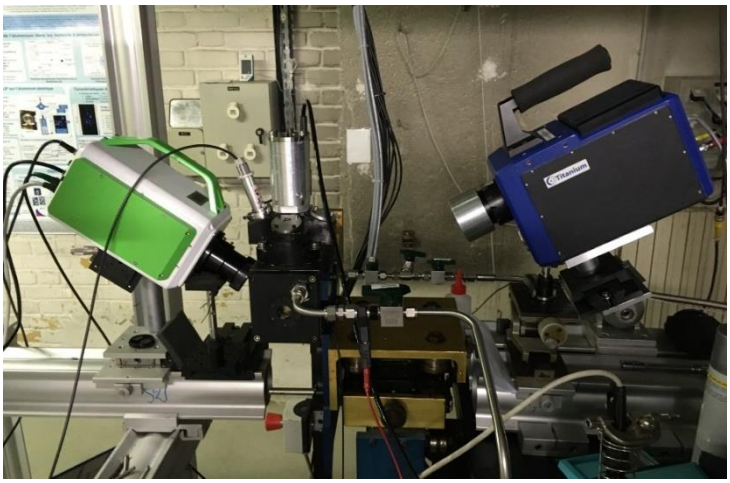

Figure 2: Combustion chamber with two IR cameras (NOXANT camera in green, FLIR camera in blue)

4.3 Experimental data analysis

4.3.1 Surface temperature calibration

T_s needs to be estimated on an absolute scale, using the signals acquired by the IR cameras (in Digital Level – DL). The cameras are calibrated using a black body source. The BC surface emissivity ε_s is also taken into account so that camera signal levels are converted properly in temperature scale. The uncertainty on the estimated ε_s was found around ± 20 %, equivalent to a temperature uncertainty below ± 12 % because of the steep temperature dependence of luminance. A more complete uncertainty analysis will be performed in the future, extending the first approach used in [19].

Figure 3 shows an example of DL curves recorded for a sample ignition test. Each curve corresponds to a different point on the sample surface so that all the curves illustrate the ignition dispersion on the sample. The first and second points that saturate the camera are highlighted with red and green respectively and their corresponding frames can be spotted on the horizontal axis (respectively 325 and 328). The selection of this first point is explained in section 4.3.2.

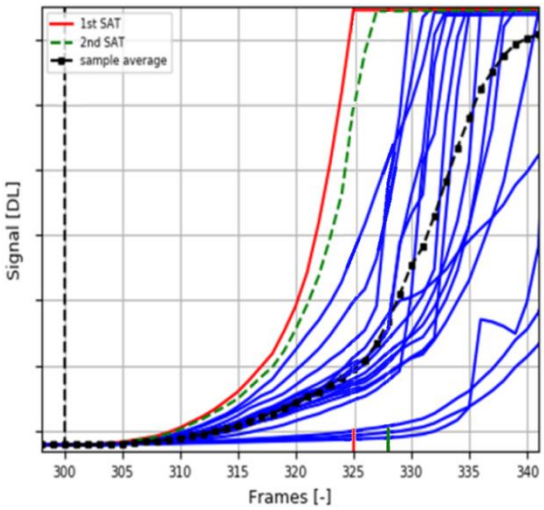

Figure 3: DL measured for different points on the sample surface.
The red curve corresponds to the first ignition point (first to saturate the camera), the one in green dashes corresponds to the second ignition point (second to saturate the camera).

4.3.2 Selection of the ignition points and estimation of the ignition delay

Ignition of a SP results from the combination of two heterogeneities. First, the BC is composite, formed of micrometric grains of different sizes. It is likely that the ignition corresponds first to a local ignition rather than a mass ignition of a very large portion of the surface. Moreover, the laser beam is itself heterogeneous, because its power density follows a Gaussian profile [34].

It is therefore interesting to study specific points on the sample surface, rather than a spatial average. Figure **4** shows 4 consecutive images of the surface heating. Two brighter points appear, leading ultimately to inflammation in two specific local areas.

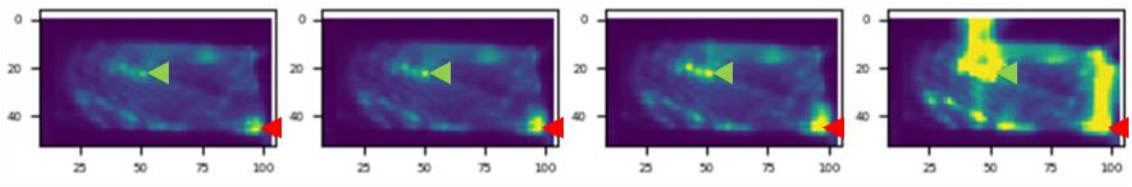

(a) (b) (c) (d)

Figure 4: Visualization of the first ignition points on a sample surface on 4 consecutive images from (a) to (d), with normal release of hot gases in image (d). Red and green triangles respectively correspond to first and second ignition points

The objective of these ignition tests is thus to isolate such local ignition points. A criterion based on the DL saturation was defined to identify automatically the ignition spots.

Selecting the first ignition point has two advantages. It makes it possible to have a point whose ignition has only been triggered by laser heating, and not by flame propagation on the surface or induced by a heat input generated by a neighboring flame that appeared earlier.

In order to reduce bias due to camera saturation, t_{ign} was estimated as a time of visualization of a flame above the sample and not only at the surface. A rectangle is thus defined in the gas zone above the sample, whose width is the same as the latter. The rectangle appears in white dotted lines in Figure 5 images. This figure presents an images sequence from the first saturation on the surface (see Figure 5a) to full flame establishment (see Figure 5f). Figure 5b corresponds to the first flame in the control rectangle above the green triangle. Thus, it is identified as the ignition delay t_{ign} for the ignition point at the green rectangle. Then, the flame progressively fills the width of the control rectangle from Figure 5d to f, illustrating the progressive ignition of the surface.

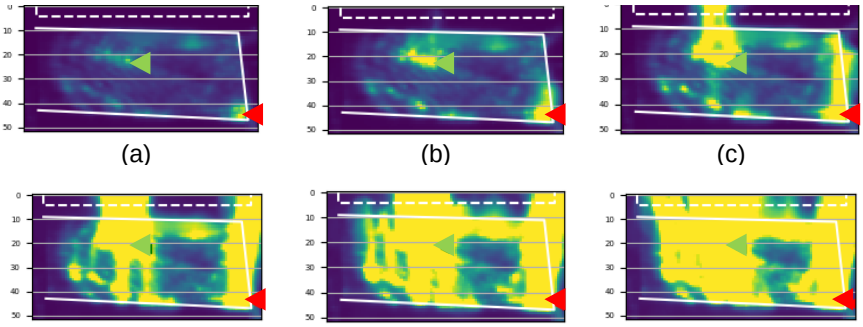

(a) (b) (c)

(d) (e) (f)

Figure 5: Progressive appearance of the flame above the sample surface from (a) to (f). The dotted rectangle corresponds to the zone above the sample where flame appearance is detected

4.3.3 Estimation of the absorbed flux by the surface

In addition to T_s, the precise estimation of the laser flux Φ_{laser} absorbed by the surface is essential for the analysis. To do so, the inert heating phase is analyzed, recalling the explicit formula for the surface temperature $T_s(t)$ in the case of a semi-infinite medium subjected to a constant heat flux Φ_{laser} in equation (1).

If the assumptions for the semi-infinite model hold, Φ_{laser} can be estimated simply using the slope of T_s plotted against $t^{0.5}$. An example of two plots $T_s(t)$ and $T_s(t^{0.5})$ are shown in Figure 6a and b. The $T_s(t^{0.5})$ plot does not show perfect linearity, at least in the first instants of heating. It can be attributed to slight synchronizing uncertainty or a possible delay for the laser to reach constant heat flux.

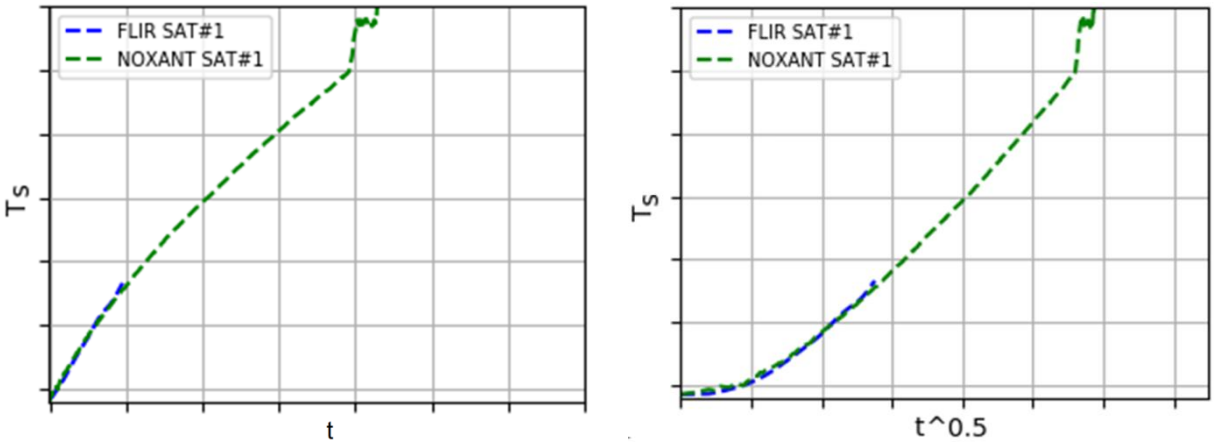

Figure 6: Evolution of T_s as a function of time t (a) and of the square root of time $t^{0.5}$ (b)

Even though there are some uncertainties in the approach, Figure 6b shows that the $t^{0.5}$ dependence is a reasonable assumption over the major portion of the heating phase. The difference between the experimental temperature evolution and the model with $t^{0.5}$ for the high temperatures probably comes from the initiation of pyrolysis leading to ignition of the sample.

A more complete uncertainty analysis on the laser flux estimation is described in [19]. It includes the impact of the camera frame rate and the initial laser trigger instant. This uncertainty linked to the instant of laser triggering is thus reported in the form of an error bar on the laser flux absorbed by the surface (see Figure 8).

The estimation of the absorbed laser flux using the slope of $T_s(t^{0.5})$ also requires knowing the values of the thermal properties of the material (λ the thermal conductivity, ρ the density and c the heat capacity). These values have been characterized by Nexter Munitions and DGA TT.

4.4 Experimental results

The different tests that were performed enabled to obtain results with a wide range of Φ_{laser} and t_{ign}. For all the tests, almost 50 ignition points were extracted based on the procedure described in section 4.3.2 and 24 of them were analyzed completely. These points are indicated in thick green for the NOXANT camera in Figure 8 ("*high T*").

4.4.1 Surface temperature evolutions

The $T_s(t)$ curves are given in Figure 7 for different values of Φ_{laser} (highest in red, intermediate in blue and lowest in green). The network of the $T_s(t)$ curves shows good consistency: the steepest curves

lead to the fastest ignitions, without barely any crossing of the curves. This denotes reproducible behavior with no random characteristic other than the local level of Φ_{laser}.

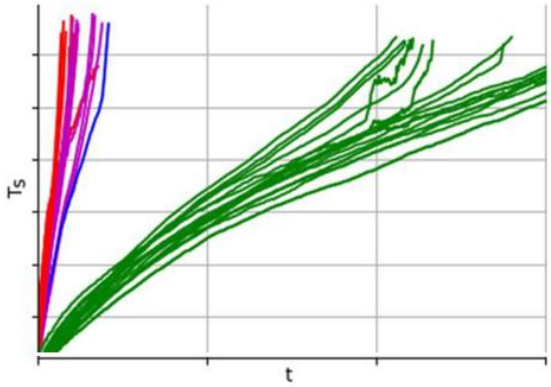

Figure 7: Evolutions of T_s for different Φ_{laser} (red for fastest ignitions, blue for intermediate ignitions and green for longest ignitions)

4.4.2 Law for t_{ign} vs Φ_{laser}

Finally, Figure 8 shows all the data from the extracted ignition points in the diagram (Φ_{laser}, t_{ign}). It globally confirms the direct correlation between these two parameters. Traditionally in SP ignition studies, the diagram is plotted with logarithmic scales along the two axes. It can be seen that the different points are linearly organized, represented by a power law as:

$$t_{ign} = k \times \Phi_{laser}^{\ p} \tag{2}$$

where k and p are constants determined thanks to a linear regression applied on the points in Figure 8. The plotted green trend is mainly built with the thick green points from the NOXANT camera ("*high T*"). Such a power law will be useful for ignition modeling in section 7.3.

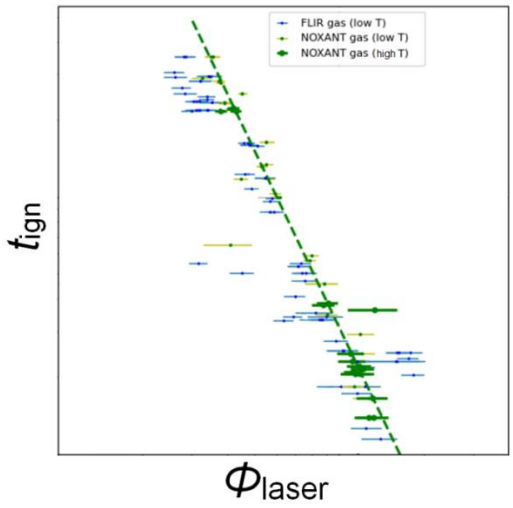

Figure 8: Diagram representing the ignition delay t_{ign} as a function of the absorbed laser flux Φ_{laser} by the BC samples. The green dotted line symbolizes the power law trend

4.5 Conclusion on the ignition study on BC small samples

This section described a procedure to analyze ignition results of BC small samples. The experimental setup and diagnostics enabled to obtain evolutions of T_s during small samples ignition under a laser flux. A power law giving t_{ign} as a function of Φ_{laser} was also determined. These two results will be used in section 7 to first find suitable parameters for the ignition model and second to compute BB ignition in IB conditions.

5 Measurement of BC regression rate at high pressure

Experimental tests were performed at DGA TT with small samples of the BC in a High Pressure Vessel (HPV) of 108 cm^3 to determine its regression rate at high pressure. The studied pressure range is above 100 MPa, corresponding to the highest pressures seen by the BB during IB. The majority of the tests were conducted with BC samples at ambient temperature (21°C). Additional tests were conducted with different initial temperatures (-40°C and 63°C) of the BC samples to study the effect on the regression rate. For these additional tests, the BC samples were put in a climatic chamber for at least 6 hours. For each test, between 3 and 6 small samples were used (see Figure 9).

Figure 9: Small BC samples used to study the regression rate in the HPV

Before each series of tests with BC samples, a preliminary « heating test » was performed with an adapted powder to heat the HPV walls. Previous experiments showed that the results reproducibility between series of tests was improved with such a preliminary heating test. The highest density allowed in the HPV is 560 kg/m^3, which leads to a maximum mass of 60 g. That is why not more than 6 samples were burnt at the same time in the HPV. 60 samples were available and 15 tests were performed (11 tests at 21°C, 2 tests at -40° C and 2 tests at 63°C). A Kistler pressure sensor is used to record the pressure evolution in the HPV and determine the maximum pressure P_{max} (see Figure 10 for typical pressure evolutions). With P_{max} and the initial density Δ in the HPV, it is possible to plot in the Amagat diagram (see Figure 11) the curve $P_{max}/\Delta = \eta \times P_{max} + f$, where η and f are respectively the covolume and force of the BC. It can be seen that a linear trend is obtained in Figure 11, meaning that constant values for η and f can be determined. The force corresponds to the energy released by the combustion of 1 kg of matter in a constant volume of 1 m^3.

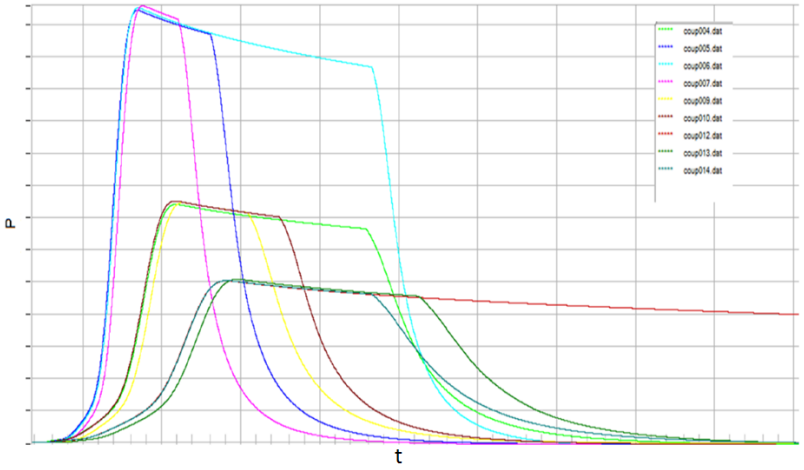

Figure 10: Pressure evolutions vs time for 9 tests in the HPV

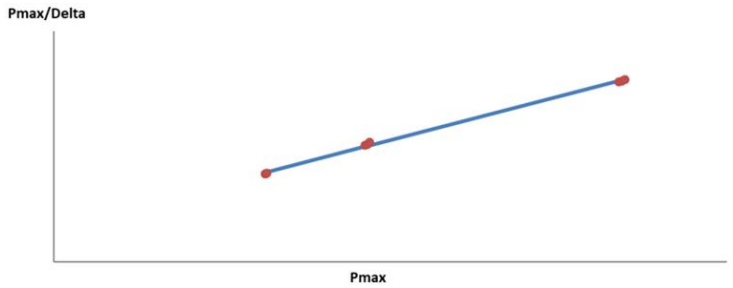

Figure 11: Amagat diagram to determine the covolume and force of the BC

Finally, the BC regression rates vs pressure are plotted for 3 initial temperatures and compared in Figure 12. As usual, it can be noticed that the higher the temperature, the higher the regression rate. Regression rates (thickness d*e* burnt during a time interval d*t*) can be expressed as $de/dt = a \times P^n - b$, where *a*, *b* and *n* are constants determined from experiments and depending on the initial temperature. However in the CFD computations, tabulations of the measured regression rates vs pressure are practically used. As a partial conclusion of this section, it can be said that the measured η and *f* will be used in the following CFD computations of BB ignition, as well as the measured regression rates.

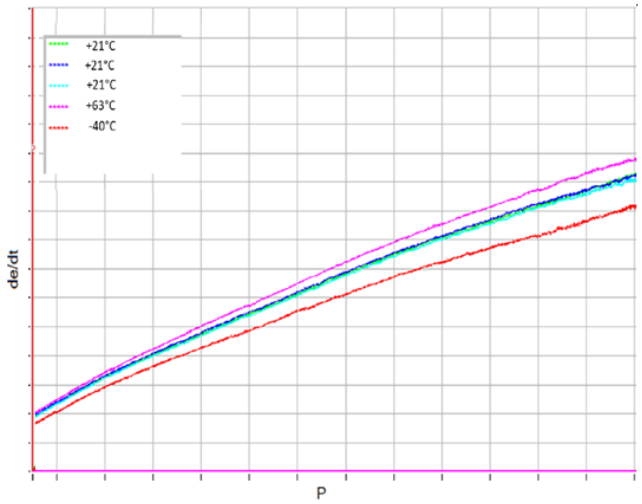

Figure 12: Comparison of the BC regression rates vs pressure for 3 initial temperatures of the samples

6 Attempt to study BB operation in the IS

6.1 Experimental setup

The third experimental characterization was performed on the IS of Nexter Munitions at Bourges [7]. Its purpose is to study the ignition phase of future and existing propulsion systems. The objective of these tests was to characterize the BB operation during the first moments of IB. Figure 13 shows a sectional view of the BB assembly: the annular BC in blue and its inhibitor sheath on its outer surface in black.

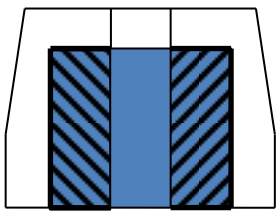

Figure 13: Sectional view of the BB assembly with the BC in blue and its inhibitor sheath in black

A schematic design of the IS is shown in Figure 14. It consists of a frame specifically designed to support the whole system. The IS usually makes it possible to visualize the ignition of the propellant charges (here 3 in Figure 14), in a chamber representative of a cannon. Visualization of the ignition process of the charges (also called modules) is possible through the filament wound that constitutes the chamber. Pressure evolutions at different positions in the chamber can be measured thanks to 3 pressure sensors as shown in Figure 14 (from P1 to P3). P1 is located at the breech, P3 at the base of the shell and P2 at an intermediate position.

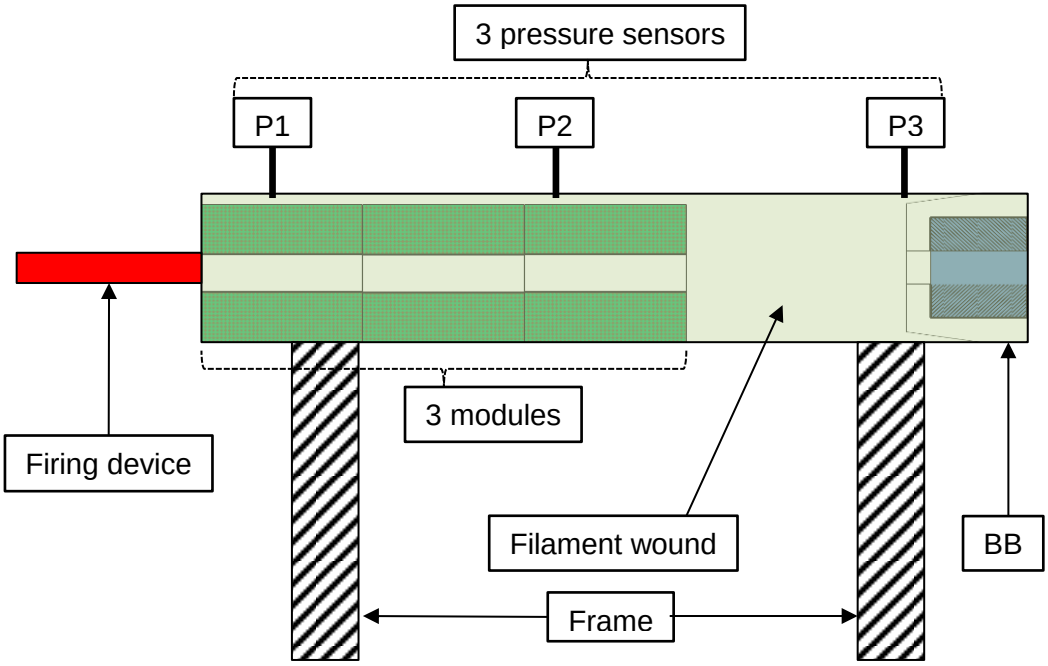

Figure 14: Sectional view of the IS showing 3 modules and the filament wound in green, the firing device in red and the BB containing the BC in blue

It is essential to note that the representativeness of the IS operation is only valid for the very beginning of the IB cycle, from the firing instant t_0 to the instant when the forcing pressure of the shell associated with the selected modules is reached. Beyond the forcing pressure and until the rupture pressure of the filament wound is reached, the interpretation of the pressure measurements remains uncertain. Indeed, the chamber volume remains constant during the tests while in real conditions the shell has already moved, therefore increasing the available volume for the powder gases produced by the combustion of the modules. The number of modules in the chamber can vary from 1 to 6. An example of modules stacked in a filament wound is depicted in Figure 15.

Figure 15: Stack of modules in a filament wound

The objectives of this experimental attempt were to measure pressure evolutions within the filament wound and visualize the behavior of the modules as well as the BB.

6.2 Experimental results

Multiple tests were performed with 3 to 5 modules. Among these tests, some led to uncomplete combustion of the BB, which enabled to estimate the consumed mass during the tests.

Typical pressure evolutions recorded for a test are displayed in Figure 16. It can be seen that at the beginning of IB, the 3 curves are very similar, until the filament wound breaks and pressures start to decrease notably. The instants indicated by the letters (c) and (d) in Figure 16 correspond to the instants of images in Figure 17c and d.

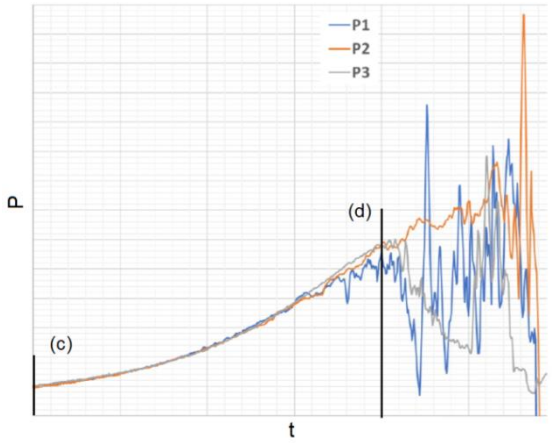

Figure 16: Typical pressure evolutions recorded

For the same test, a high-speed camera enabled to record the different steps of the IB beginning: the ignition of the propellant charges (see Figure 17a) followed by the dislocation of the modules leading to intense heat release (see Figure 17b), then the start of the pressure rise in the filament wound due to modules combustion (see Figure 17c) and finally the breaking of the latter (see Figure 17d). When pressure starts rising notably, the BB ignition and combustion cannot be distinguished from the modules combustion.

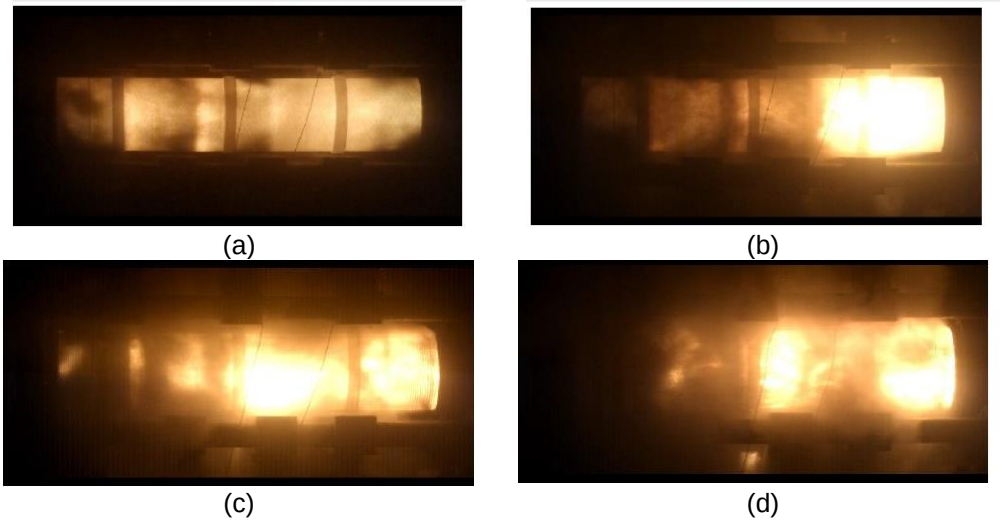

Figure 17: Pictures recorded by the high-speed camera for a test. (a) Modules ignition, (b) dislocation of the modules, (c) start of the pressure rise, (d) breaking of the filament wound

6.3 IB computations based on experimental data

In this section, some IB computations were performed by Nexter Munitions with a numerical tool based on a two-phase flow modelling adapted to IB [3]. Numerical results are then compared to the experimental pressure evolutions from a test. The objective of these computations is to obtain

pressure and temperature evolutions at the BB base to be used in section 7 for BB ignition computations in IB conditions with a CFD tool.

First, it is interesting to see in Figure 18 that the pressure evolutions recorded in the IS for several tests are not so far from the cannon shot evolution. It confirms that the IS is able to reproduce the first instants of the IB cycle.

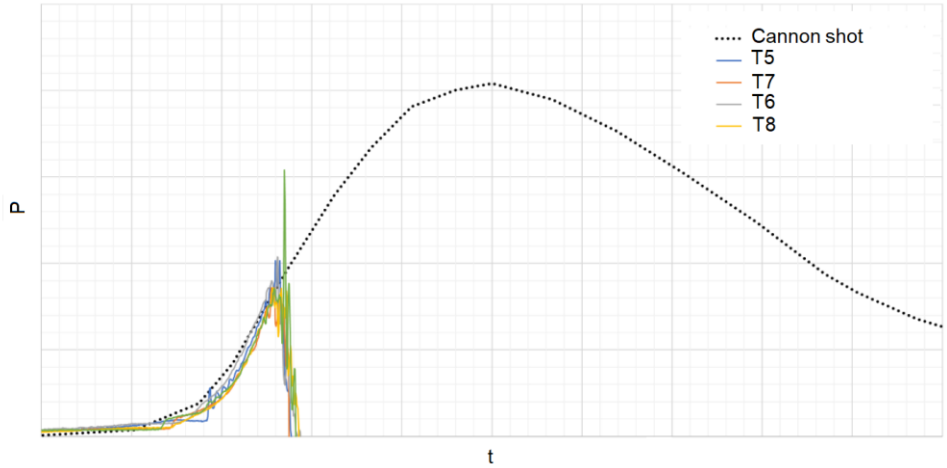

Figure 18: Comparison of pressure evolutions in the IS (T5 to T8) with a pressure evolution from a cannon shot

Figure 19 shows a comparison between computed pressure evolutions and a pressure evolution from a cannon shot. The computations were adjusted to obtain nearly the same values of maximum pressure and exit velocity at the cannon muzzle with slightly different parameters. Although some differences can be noted, the pressure evolutions are similar. The computed pressure evolution as well as the temperature one will be used in section 7.

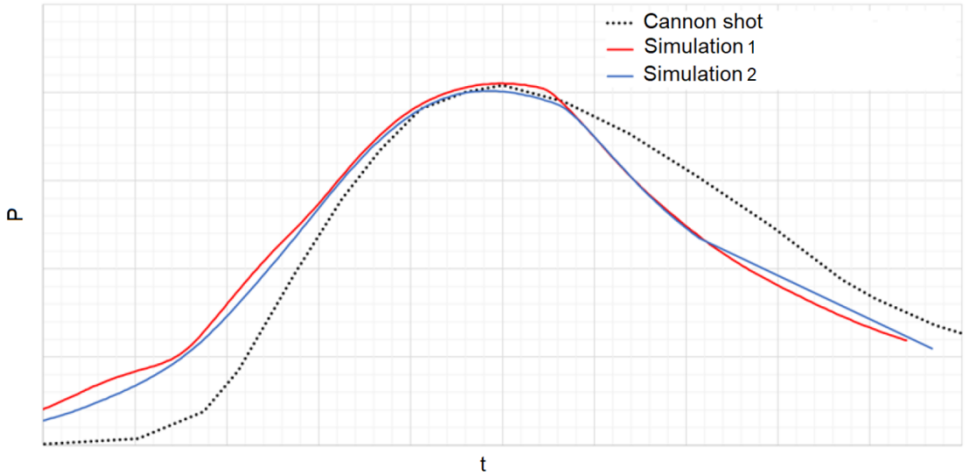

Figure 19: Comparison of a computed pressure evolution in IB with a pressure evolution from a cannon shot

6.4 Conclusions on the IS experiments

The IS tests campaign did not reveal any particular behavior of the BB in the first moments of the IB cycle. Most of the time, the BC is completely burnt at the end of a test. On the high-speed camera, it is difficult to visualize the BC combustion as soon as all the modules ignite and burn. Also when the filament wound breaks, it is not possible to visualize how and when the BC combustion ends.

Some perspectives can be drawn from these experiments such as improving the diagnostics to better follow the BB ignition, combustion and potential extinction.

7 Numerical simulation of BB ignition in IB

This last section is dedicated to the numerical simulation of BB ignition in IB conditions. The simulations are performed with the CEDRE code developed at ONERA, DMPE [35]. General background, thermodynamic properties, meshing techniques and boundary conditions will be successively described. Finally, results regarding BB ignition in IB conditions will be provided.

7.1 Numerical procedure

7.1.1 The CEDRE code

CEDRE [35] is a multiphysics software developped by the PLM (*Multiphysics Platform*) team from the DMPE (*Multiphysics for Energetics Department*) of ONERA. It contains multiple solvers dedicated to particular physics (gaseous flow, two-phase flow, radiation, film streaming and heat transfer in solids) that can be coupled. In this study, only the gaseous solver CHARME will be used. CHARME enables to solve the Navier-Stokes conservation equations for a compressible gas with a finite volumes discretization on general unstructured meshes. The MUSCL (Monotonic Upstream Scheme for Conservation Laws) interpolation scheme with the Van Leer slope limiter provides second-order accuracy on the convective fluxes. A central difference second-order scheme is used to compute the viscous fluxes. A first-order implicit Euler scheme and a 10^{-6} s timestep are used for time integration. In this study, turbulence modeling will be accounted for with the *k-ω* SST RANS model. Given the framework presented hereafter, a usual BB ignition computation lasts approximately 40 hours on 140 Broadwell CPU.

7.1.2 BB Geometry and meshing techniques

The considered BB geometry is given in Figure 13. Figure 20 shows the numerical domain that can be produced. The BC in the BB assembly shows an annular channel in which the powder gases will generate heat fluxes at the BC surface after the cannon shot. A small volume with an arbitrary length *L* (see Figure 20) is added at the BB base to apply properly the boundary conditions (pressure and temperature profiles) produced by the powder gases during IB. It is important to note that IB is not solved by CEDRE but its effect on the BB must be modelled (see section 7.1.3).

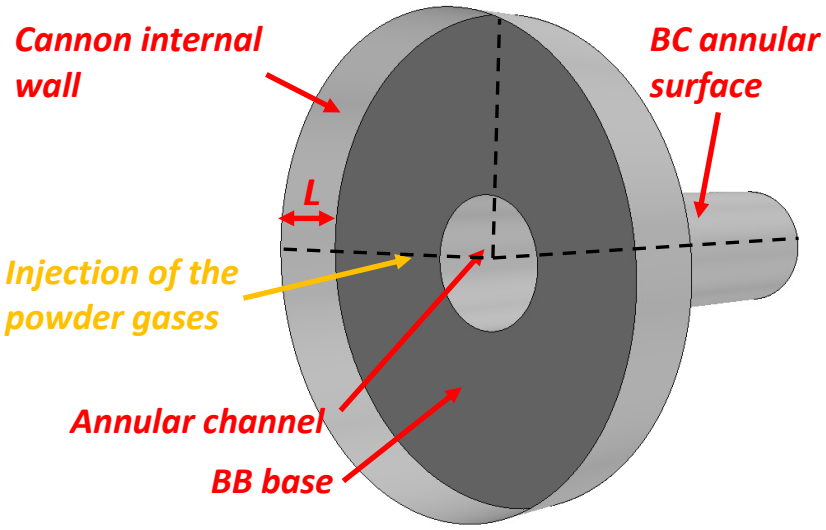

Figure 20: Geometrical domain representing the gaseous volume at the base of the BB and in the annular channel. The dashes represent the actual numerical domain on one quarter

A mesh of the geometry in Figure 20 is produced and displayed in Figure 21a. As the BB has an annular channel, the mesh is defined on only one quarter of the initial geometry and comprises around 1.2×10^6 cells for the initial mesh and 3.2×10^6 cells for a refined mesh. Some comparative pictures of the two meshes are shown in Figure 21b. It can be seen that prismatic cells with a progressively decreasing thickness down to the BC surface are used. Usually, this is performed to refine the resolution of the boundary layer and to have a more accurate evaluation of friction and heat transfer at the wall. In this study, the use of a refined mesh did not produce significant differences on the BC ignition delay and consumed mass during IB.

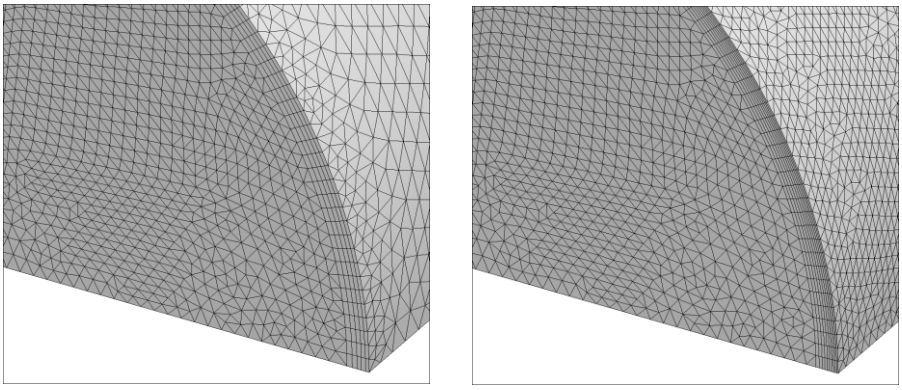

(a) (b)

Figure 21: Meshes of the numerical domain at the BC boundary in one quarter. (a) Reference mesh, (b) refined mesh

7.1.3 Accounting for IB boundary conditions

IB deals with the phenomena linked to propellant charges combustion and shell motion inside a cannon after the shot, before the shell base reaches the cannon muzzle. As IB cannot be computed by CEDRE, a code dedicated to IB computations [3] is used to reproduce the different IB phases as shown in Figure 22 and described below:

1. Propellant charges are ignited with a pyrotechnic signal.
2. Powder gases expand propellant charges burn.
3. The shell is put in motion due to high pressure application at its base.

This third step is also linked to the CEDRE computation because the resulted pressure and temperature at the base from the IB computation are used as boundary conditions in the ignition simulation with a CFD approach. Step 4 in Figure 22 is then dedicated to the flow computation of powder gases at high pressure and temperature in the BB channel to produce heat transfers at the BC surface. In this study, pressure and temperature evolutions that are applied at the BB base are given in Figure 23.

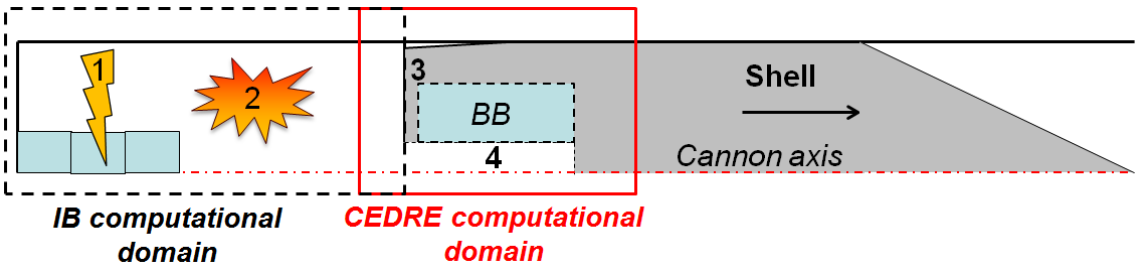

Figure 22: Procedure used to couple IB results to CFD computation of a BB ignition

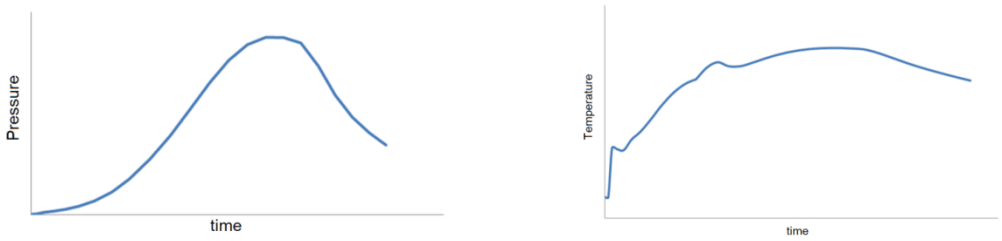

(a) (b)

Figure 23: Pressure (a) and temperature (b) evolutions generated at the base of the BB for IB

7.2 Thermodynamic properties of gases

7.2.1 Equation of state for a real gas

As IB is considered, pressure above 100 MPa are usually dealt with, meaning that real gas effects should be accounted for. In this study, they are introduced with a van der Waals equation of state:

$$\left(P+\frac{a_c}{v^2}\right)(v-\eta)=\frac{RT}{W} \tag{3}$$

where a_c is a cohesion term, η is the covolume, R is the universal gas constant, W is the molar mass. In this framework, a_c et η can be linked to the critical pressure and temperature (P_c, T_c) such as:

$$a_c=\frac{27R^2T_c^{\,2}}{64P_cW^2} \tag{4}$$

$$\eta=\frac{RT_c}{8P_cW} \tag{5}$$

It can be noticed that for high pressures, the cohesion term becomes negligible and the expression (3) tends to the Noble-Abel law, which is also commonly used in IB applications. Going back to the Amagat diagram in Figure 11 and the expression of $P_{max}/\Delta = \eta \times P_{max} + f$, it can be seen that the force f can be identified as RT_f/W, where T_f here stands more particularly for the flame temperature reached by a burning composition at equilibrium.

7.2.2 BC burnt gases

A thermochemical equilibrium is computed with a dedicated in-house code to determine the characteristics (composition, flame temperature) of the BC burnt gases. As no combustion kinetics is accounted for in the CFD, BC burnt gases are directly injected at the BC surface after ignition. Then, it is interesting to use an equivalent gas that is defined as one equivalent fictitious species representing the BC burnt gases with the same averaged properties (W, c_p, μ, λ). This numerical artefact is used to strongly limit the computational cost when it is possible. Some of the obtained thermodynamic properties for the equivalent gas are represented in Figure 24. Figure 24a shows a typical Sutherland profile for the dynamic viscosity as a function of temperature.

(a) (b)

Figure 24: Dynamic viscosity (a) and heat capacity (b) profiles as functions of temperature for the equivalent gas representing the BC burnt gases

The other important data given by the equilibrium computation is the flame temperature T_f. Following the discussion regarding the relationship between f and T_f in section 7.2.1, it has been found a good consistency between f computed from T_f and W given by an equilibrium computation, and f given by the experimental plot in the Amagat diagram from Figure 11. T_f is then used as a boundary condition for the BC burnt gases once the surface has been ignited. As a van der Waals equation of state is chosen, P_c and T_c must be prescribed. As η has been experimentally determined with the Amagat diagram, it can be linked to these critical values with equation (5).

7.2.3 Powder gases

An example of a powder gases composition can be found in [36]. In this reference, the dominant species is CO with more than 50% in mass. To simplify the present ignition simulations, it is assumed that the generated powder gases are composed entirely of CO. The thermodynamic properties of CO (W, c_p, μ, λ, P_c, T_c) used for the computations come from regular thermodynamic tables.

7.3 Ignition modelling

7.3.1 Model basis

The ignition phenomenology of a SP has been described from an experimental point of view in section 4.1. The principles of the numerical framework adopted here are presented in Figure 25 and can be described as follows:

- First, the inert surface is gradually heated by a flux that may come from various sources (radiative flux from a laser in section 4, convective flux from the powder gases in section 6 and 7.4.2). It is assumed that the heat flux is entirely absorbed at the surface and then that heat diffuses normally into the SP, from the surface to the boundary condition. The thermal profile in the SP is then updated, at each time step, given the current surface heat flux, the previous thermal profile and the diffusivity of the SP.
- Second, T_s gradually increases and the mass flow rate $\dot{m}$ produced by the SP regression as a function of T_s is evaluated according to a pyrolysis law of the Arrhenius form:

$$\dot{m} = \rho_p A_p \exp\left(\frac{-E_p}{R T_s}\right) \tag{6}$$

  as it is usually done in SP ignition studies [21]. ρ_p is the SP density, E_p is the activation energy of reactions in condensed phase and A_p is a pre-exponential constant.

- Then, when the SP is fully ignited, the contribution of the convective flux at the wall decreases in favor of the flux produced by the flame, which is computed without any kinetic mechanism. The reactions taking place in the condensed phase in the SP are taken into account according to a heat of reaction Q_s, which does not distinguish the contribution of phase transitions from pure chemical reactions.
- In steady combustion mode, $\dot{m}$ reaches the expression given by Vieille's law:

$$\dot{m} = \rho_p v_0 \tag{7}$$

  v_0 is the regression rate given by Figure 12. The BB burnt gases are released at T_f which is evaluated by the equilibrium computation (see section 7.2.2).

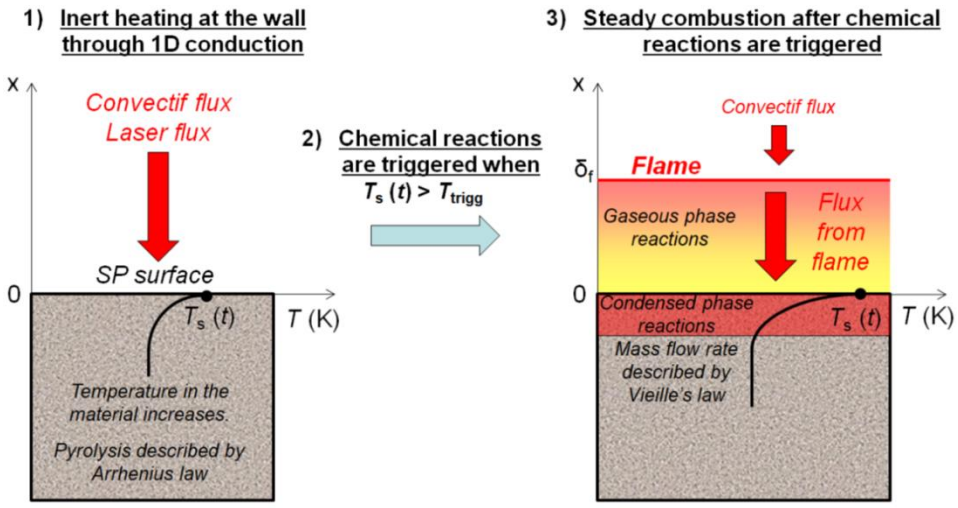

Figure 25: Ignition modelling principles

7.3.2 Determination of the model parameters

The ignition parameters of a SP are the 3 thermal properties defining thermal diffusivity and then the 3 parameters introduced in section 7.3.1. The thermal properties can be usually measured easily. The remaining 3 parameters can be determined with an optimization process based on experimental results ($T_s(t)$ curves and law for the ignition delay). In this study, the process was simplified so that Q_p and E_p were fixed based on authors experience and then only A_p was determined with an iterative procedure according to section 7.4.1.

7.4 Ignition simulations

7.4.1 Validation cases for a small sample ignition

First simulations of BB ignition tended to confirm that the heat flux received at the BC surface is around a few MW.m^{-2}. The objective of this section is to optimize the choice of A_p so that the corresponding numerical t_{ign} and $T_s(t)$ curves match the measured ones for this heat flux range.

Figure 26 shows a comparison between experimental and numerical $T_s(t)$ for 4 heat fluxes. The ignition delay t_{ign} can be spotted on the "model" curves when a sudden temperature rise is seen. On the "measure" curves, it is spotted when the evolution stops because it also corresponds to a sudden temperature rise and consequently leads to camera saturation.

Figure 26a deals with a low heat flux. In that case, the model predicts a faster ignition delay with a fairly good comparison of the curves before ignition. Then, Figure 26b shows that for an intermediate heat flux, t_{ign} is well computed, as well as the $T_s(t)$ curve. Figure 26c and d are related to higher heat fluxes. Again, t_{ign} seems well evaluated.

After these tests, some confidence has been gained regarding the choice of the parameters of the ignition model. The model will be now tested in the following section on a BB ignition case.

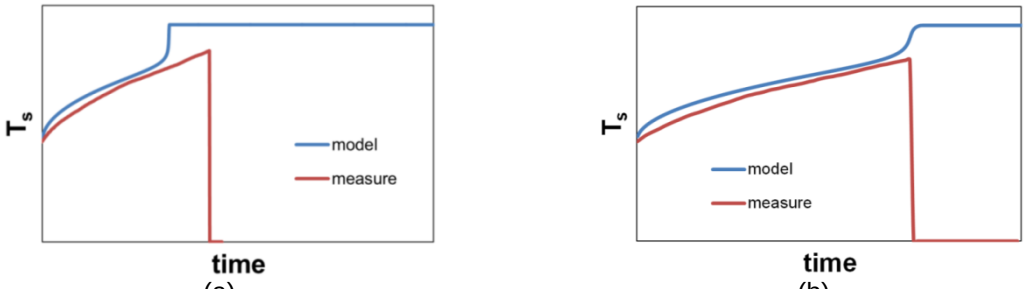

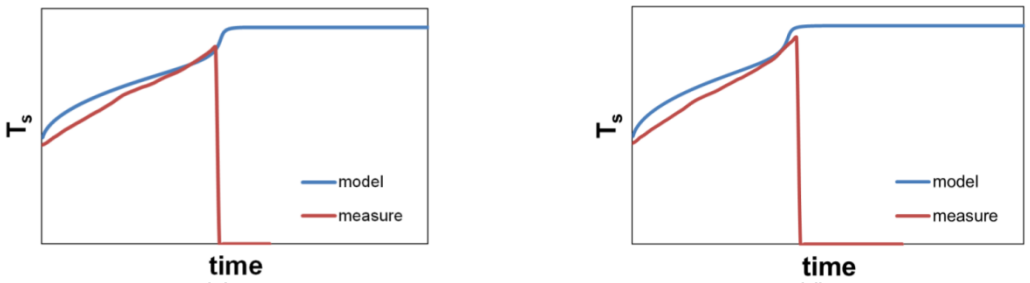

Figure 26: Comparisons of the computed and measured T_s evolutions for different absorbed heat fluxes. (a) Low heat flux, (b) intermediate heat flux, (c) and (d) higher heat fluxes

7.4.2 Ignition simulation of a BB during IB

The numerical procedure has been introduced in section 7.1. The powder gases are injected according to unsteady boundary conditions determined by IB computations (see Figure 23). The convective heat flux produces an increase in the BC surface temperature up to a temperature threshold, until ignition is triggered. This unsteady heating process is shown in Figure 27 with the convective heat flux first, and in Figure 28 with the flame flux and T_s. The figures are represented with a horizontal mirror view from the initial domain on one quarter. At the beginning, the heat flux is rather low (see Figure 27a) but keep increasing when the powder gases are injected into the BB channel (see Figure 27b). Then, when ignition begins, the contribution of the convective heat flux to heat the BC surface decreases (see Figure 27c) whereas the contribution from the flame flux increases (see Figure 28c). It is assumed here that when the surface is ignited, the flame flux sustains the SP regression and not the convective flux anymore. Simultaneously, T_s increases (see Figure 28a). At the end of the ignition process, the convective flux continues heating the BC surface at its inlet (see Figure 27d). The flame flux acts on the majority of the BC surface (see Figure 28d) and T_s has almost reached the threshold value everywhere (see Figure 28b). Figure 29 finally enables to represent the mass flow rate produced by the BC after ignition. The red isosurface corresponds to the BC burnt gases that are emitted toward the BB outlet.

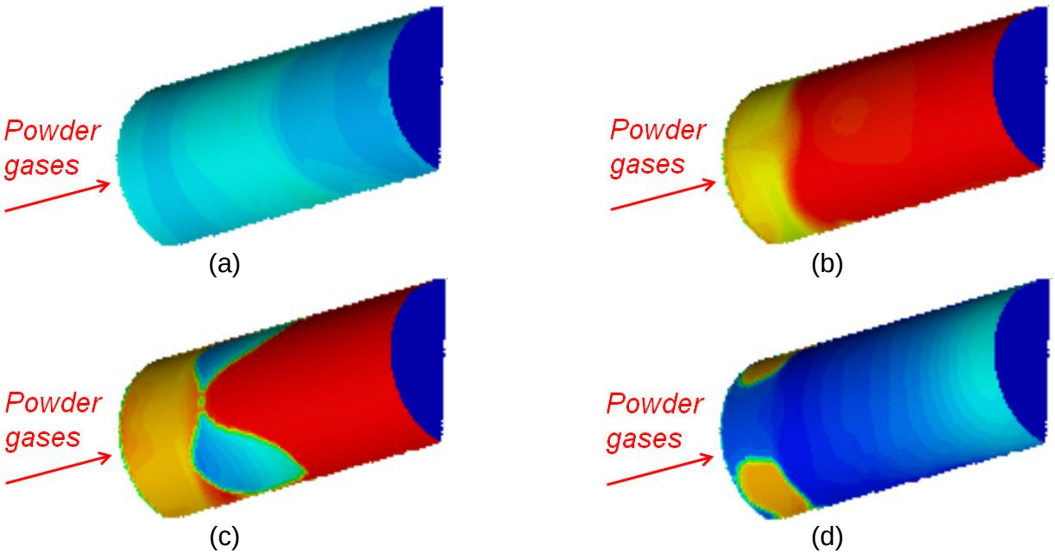

Figure 27: Convective heat flux from the powder gases at the BC surface for 4 instants. (a) Beginning of heating, (b), heating with a high heat flux, (c), beginning of ignition, (d) end of complete ignition

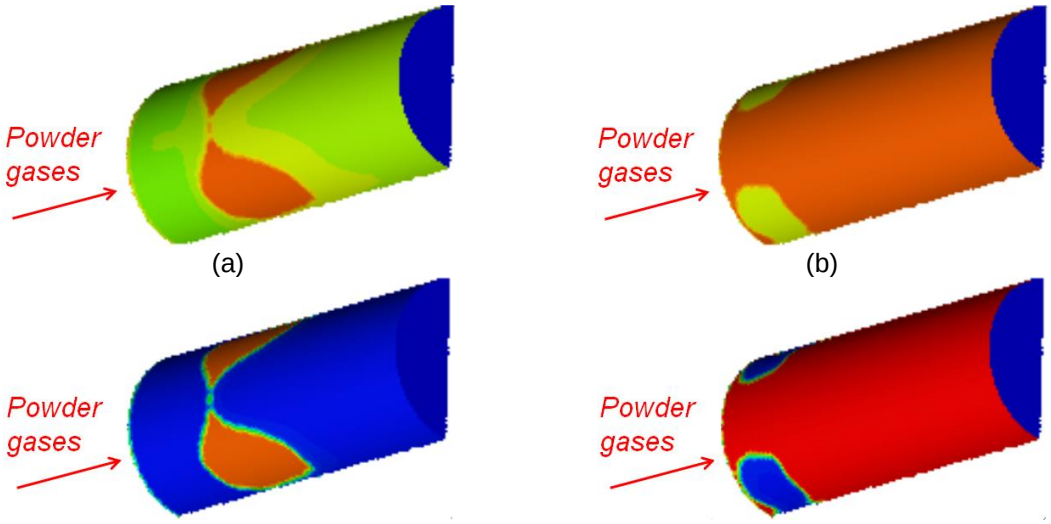

Figure 28: Visualization of T_s ((a) and (b)), and the flame flux ((c) and (d)) at the beginning (left) and end of ignition (right)

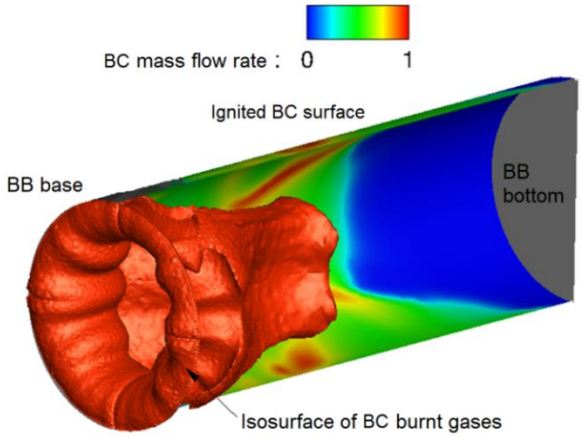

Figure 29: Isosurface representing BC burnt gases produced during BB ignition

After having studied the ignition conditions of the BC, it is interesting to determine the initial BC mass that has been consumed during IB. Figure 30 shows the evolution of the produced dimensionless mass flow rate as a function of a dimensionless time representing IB duration. It can be seen that the mass flow rate starts increasing at about 10% of the total IB duration. Then, the mass flow rate evolution is very similar to the pressure one in Figure 23a. This is expected since the regression rate is usually proportional to pressure.

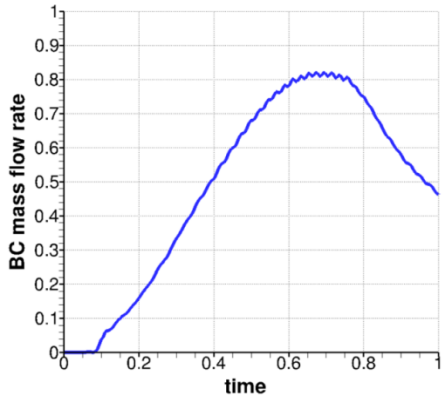

Figure 30: Mass flow rate produced during IB after BC ignition

7.5 Conclusion on the numerical simulations

This last section enabled to use all the previous experimental results to perform a BB ignition simulation. In particular, the physical parameters of the ignition model have been determined thanks to ignition delay measurements on small samples and the regression rate of the BC has been measured in a HPV. This last measure also gave the possibility to adjust the parameters of the real gas equation of state.

Given the annular configuration of the BB, the numerical domain was reduced to one quarter of the entire domain. The boundary conditions needed to generate a powder gases flow in the BB channel were obtained with a dedicated IB computational tool. Although subject to uncertainties, the ignition model makes it possible to provide reasonable predictions of the remaining BC mass when the shell gets out of the cannon. Then, these results can be used to simulate the BB operation in external ballistics and to determine its contribution along a shell trajectory.

8 General conclusion

The objectives of this study were to determine the ignition capacity of a BC and to determine the consumed mass of the BC during IB. To do so, multiple experimental characterizations were performed on a BC. In particular, a law for t_{ign} as a function of Φ_{laser} was obtained, as well as T_s profiles for BC samples under a laser flux. Also, the regression rate of the BC was measured in a HPV to determine the BC consumption in IB conditions. Moreover, BB operation was studied in the IS and some experiments enabled to obtain partial consumption of the BC. All of these experimental data made it possible to perform CFD of the BC ignition and consumption in IB conditions, with high pressure and temperature powder gases providing high heat fluxes at the BC surface.

The following steps of this study can be dedicated to comparisons of the BC consumptions rates in experiments and simulations, and to the improvements of both the experimental and numerical procedures to determine BC consumption during IB.

9 Acknowledgements

The authors would like to express their thanks to Jimmy Knockaert from DGA TT, who measured the BC regression rate in the HPV. This study was funded by DGA TT.

10 References

[1] *Krier, H., & Summerfield, M. (1979). Interior ballistics of guns. Progress in astronautics and aeronautics, 66.*

[2] *Gough, P. S., & Zwarts, F. J. (1979). Modeling heterogeneous two-phase reacting flow. AIAA Journal, 17(1), 17-25.*

[3] *Della Pieta, P., & Reynard, C, Numerical investigation for modeling interior ballistics two-phase flow in: Proceedings of the European Forum on Ballistics of Projectiles, April 2000, pp. 137-148.*

[4] *Nussbaum, J., Helluy, P., Herard, J. M., & Baschung, B. (2011). Multi-dimensional two-phase flow modeling applied to interior ballistics. Journal of Applied Mechanics, 78(5).*

[5] *Jang, J. S., Oh, S. H., & Roh, T. S. (2016). Development of three-dimensional numerical model for combustion-flow in interior ballistics. Journal of Mechanical Science and Technology, 30, 1631-1637.*

[6] *Cayzac, R., Carette, E., de Roquefort, T. A., Renard, F. X., Roux, D., Patry, J. N., & Balbo, P. (2011). Computational Fluid Dynamics and Experimental Validations of the Direct Coupling Between Interior, Intermediate and Exterior Ballistics Using the Euler Equations. Journal of Applied Mechanics, 78.*

[7] *Legeret, G., & Orsat, G. (2016, May). New Generation Ignition Simulator Device. In 29th International Symposium on Ballistics.*

[8] *Wildegger-Gaissmaier, A. E., & Johnston, I. R. (1996). Ignition of a granular propellant bed. Combustion and flame, 106(3), 219-230.*

[9] *Bull, G. V. (1991). Base Bleed Technology in Perspective. International Journal of Energetic Materials and Chemical Propulsion, 1(1-6).*

[10] *Andersson, K., Gunners, N. E., & Hellgren, R. (1976). "Swedish Base Bleed"–increasing the range of artillery projectiles through base flow. Propellants, Explosives, Pyrotechnics, 1(4), 69-73.*

[11] *Mathur, T., & Dutton, J. C. (1996). Base-bleed experiments with a cylindrical afterbody in supersonic flow. Journal of Spacecraft and Rockets, 33(1), 30-37.*

[12] *Sahu, J., & Heavey, K. R. (1997). Numerical investigation of supersonic base flow with base bleed. Journal of Spacecraft and Rockets, 34(1), 62-69.*

[13] *Kaurinkoski, P., & Hellsten, A. (1998). Numerical simulation of a supersonic base-bleed projectile with improved turbulence modeling. Journal of Spacecraft and Rockets, 35(5), 606-611.*

[14] *Bournot, H., Daniel, E., & Cayzac, R. (2006). Improvements of the base bleed effect using reactive particles. International journal of thermal sciences, 45(11), 1052-1065.*

[15] *Regodić, D., Jevremović, A., & Jerković, D. (2013). The prediction of axial aerodynamic coefficient reduction using base bleed. Aerospace Science and Technology, 31(1), 24-29.*

[16] *Rose, I., Vos, J., Gehri, A., Drag reduction through after-burning of base bleed gases in: Proceedings of the 21st International Symposium on Ballistics, Adelaide, South Australia, 19–23 April 2004.*

[17] *Xue, X., & Yu, Y. (2016). An improvement of the base bleed unit on base drag reduction and heat energy addition as well as mass addition. Applied Thermal Engineering, 109, 238-250.*

[18] *Aziz, M., Ibrahim, A., Riad, A., & Ahmed, M. Y. M. (2022). Live Firing and 3D Numerical Investigation of Base Bleed Exit Configuration Impact on Projectile Drag. Advances in Military Technology, 17(1), 137-152.*

[19] *Devillers, R., Boulal, S., Dupays, J., Rommeluere, S., & Henry, D. Quantitative experimental characterization of solid propellant surface temperature before ignition for future model validation in 9TH European Conference For Aeronautics And Space Sciences EUCASS-3AF, June 2022.*

[20] *Saito, T., Shimoda, M., Yamaya, T., & Iwama, A. (1991). Ignition of AP-based composite solid propellants containing nitramines exposed to CO2 laser radiation at subatmospheric pressures. Combustion and flame, 85(1-2), 68-76.*

[21] *Lengellé, G., Duterque, J., Trubert, J.-F. (2002). Combustion of Solid Propellants. RTO/VKI Special Course on "Internal Aerodynamics in Solid Rocket Propulsion",held in Rhode-Saint-Genèse, Belgium, 27-31 May 2002, and published in RTO-EN-023.*

[22] *Orlandi, O., Fourmeaux, F., & Dupays, J. (2019). Ignition Study at Small-Scale Solid Rocket Motor. EUCASS 2019*

[23] *Cain, J., & Brewster, M. Q. (2006). Radiative Ignition of Fine-Ammonium Perchlorate Composite Propellants. Propellants, Explosives, Pyrotechnics: An International Journal Dealing with Scientific and Technological Aspects of Energetic Materials, 31(4), 278-284.*

[24] *Zhang, L., Tian, R., & Zhang, Z. (2017). Burning rate of AP/HTPB base-bleed composite propellant under free ambient pressure. Aerospace Science and Technology, 62, 31-35.*

[25] *Shen, H., & Yu, Y. G. (2013). Study on Measurement and Simplified Model of Burning Rate of AP/HTPB Base Bleed Propellant under High Pressure. In Advanced Materials Research (Vol. 724, pp. 1176-1180). Trans Tech Publications Ltd.*

[26] *Hu, S., Chen, J., Wu, G., Xu, Q., Liu, H., & Hua, Y. (2014). Burning Behavior of Solid Propellants at High Pressure. Combustion Science and Technology, 186(12), 1858-1888.*

[27] *Mukhtar, A., Nasir, H., & Waheed, H. (2018). Pressure-time study of slow burning rate AP/HTPB based composite propellant by using closed vessel test (CVT). In Key Engineering Materials, Vol. 778, pp. 268-274, Trans Tech Publications Ltd.*

[28] *Dillier, C. A., Petersen, E. D., Sammet, T., Rodriguez, F. A., Thomas, J. C., & Petersen, E. L, Very-High-Pressure Burning Rates of AP/HTPB-Composite Propellants with Varying AP Particle Sizes and Distributions in AIAA Propulsion and Energy 2019 Forum, p. 4368.*

[29] *Atwood, A. I., Ford, K. P., & Wheeler, C. J. (2013). High-pressure burning rate studies of solid rocket propellants. Progress in Propulsion Physics, 4, 3-14.*

[30] *Beckstead, M. W., Puduppakkam, K., Thakre, P., & Yang, V. (2007). Modeling of combustion and ignition of solid-propellant ingredients. Progress in Energy and combustion Science, 33(6), 497-551.*

[31] *Gallier, S., Ferrand, A., & Plaud, M. (2016). Three-dimensional simulations of ignition of composite solid propellants. Combustion and Flame, 173, 2-15.*

[32] *Francois, L., Dupays, J., & Massot, M., A new simulation strategy for solid rocket motor ignition: coupling a CFD code with a one-dimensional boundary flame model, verification against a fully resolved approach in AIAA Propulsion and Energy 2021 Forum, p. 3695.*

[33] *Linan, A., & Williams, F. A. (1971). Theory of ignition of a reactive solid by constant energy flux. Combustion Science and Technology, 3(2), 91-98.*

[34] *Granier, J. J., Mullen, T., & Pantoya, M. L. (2003). Nonuniform laser ignition in energetic materials. Combustion Science and technology, 175(11), 1929-1951.*

[35] *Refloch, A., Courbet, B., Murrone, A., Villedieu, P., Laurent, C., Gilbank, P., Troyes, J., Tessé, L., Chaineray, G., Dargaud, J. B., Quémerais, E., & Vuillot, F. (2011). CEDRE software. Palaiseau: Aerospace Lab, 1–10.*

[36] *Zhuo, C., Feng, F., Wu, X., Liu, Q., Ma, H. (2014). Numerical simulation of the muzzle flows with base bleed projectile based on dynamic overlapped grids, Computer & Fluids, vol. 105, 307-320.*